J. Fluid Mech. (2003), *vol.* 483, *pp.* 67–89.
DOI: 10.1017/S0022112003003884 Printed in the United Kingdom

Transition mechanisms induced by travelling crossflow vortices in a three-dimensional boundary layer

By PETER WASSERMANN AND MARKUS KLOKER

Institut für Aerodynamik und Gasdynamik, Universität Stuttgart, Pfaffenwaldring 21, D-70550 Stuttgart, Germany

(Received 22 April 2002 and in revised form 6 December 2002)

The laminar breakdown induced by purely travelling crossflow vortices in a three-dimensional flat-plate boundary-layer flow is investigated in detail by means of spatial direct numerical simulations. The base flow considered is generic for an infinite swept wing, with decreasing favourable chordwise pressure gradient and a sweep angle of 45°. First, the primary downstream growth and nonlinear saturation state of a single crossflow wave are simulated. Secondly, background disturbance pulses are added, and the subsequent mechanisms triggering transition to turbulence in this scenario are identified and analysed in detail. The saturated travelling crossflow vortex is found to give rise to a co-travelling secondary instability not unlike the instability in the much investigated steady crossflow-vortex case, but with characteristic differences. An analysis method with a spanwise Galilean transformation to travel with the primary wave and a consequently adapted timewise/spanwise Fourier decomposition of the disturbance flow enables unambiguous isolation of the various secondary disturbance modes. The resulting flow structures and their dynamics in physical space are visualized.

1. Introduction

On a swept-back wing, the chordwise acceleration of the flow in the upper front part induces an inboard-oriented crossflow component inside the boundary layer perpendicular to the meanflow direction. The crossflow velocity profile $w_s(y)$, y being the wall-normal coordinate, is inflectional and causes a strong primary spatial instability of the flow with respect to so-called crossflow (CF) eigenmodes, which can be steady or unsteady. Unsteady modes have a higher maximum primary (exponential) amplification than steady modes.

For crossflow-instability dominated flows, two main different transition scenarios can be distinguished depending on the flow conditions. Unsteady CF disturbances have been found to be dominant at medium- to high-turbulence conditions, where they are excited on higher-amplitude levels and hinder the development of the unstable steady modes. At low free-stream-turbulence conditions, steady crossflow vortex modes are found to be dominant. Obviously, the steady modes which are excited even by minute surface non-uniformity or roughness start with higher amplitudes.

Most investigations concentrated on regimes with pure or still significant steady primary disturbances. This is because low-turbulence conditions are supposed to be present in free flight, but also because a steady primary scenario is more tractable. Most experimental work on the subject, employing controlled experiments with

well-defined artificial disturbance input, has been done by three groups: at DLR Göttingen, Germany, by Bippes, Deyhle, Lerche and co-workers; at the unsteady wind tunnel facility of the Arizona State University (ASU) by Saric, White and others (for reviews, including work of others, see Bippes 1999 and Saric, Carrillo & Reibert 1998); and at Tohoku University, Sendai, by Kohama, Kodashima & Watanabe (1995) and Kawakami, Kohama & Okutsu (1999). In parallel, a number of theoretical investigations on this topic have been performed. Typically, the parabolized stability equations (PSE) are used to calculate nonlinear states of the primary unstable steady crossflow modes, see, e.g. Malik, Li & Chang (1994), Malik *et al.* (1999), Haynes & Reed (1996, 2000), Janke & Balakumar (2000) and the more general review by Reed, Haynes & Saric (1998). Koch *et al.* (2000) additionally use nonlinear equilibrium solutions. Subsequently, Floquet theory is employed for a temporal secondary instability analysis to identify the most amplified secondary instabilities. The theoretical studies have been continued by Koch (2002). Furthermore, several investigations by means of direct numerical simulations (DNS) have been carried out. Various DNS using the temporal model were performed by Kleiser and co-workers, lately by Wintergerste & Kleiser (1996, 1997). The computationally more demanding and physically more sound spatial model has been used by Högberg & Henningson (1998) and in our former investigations (Wassermann & Kloker 2002). The results of the latter work agree well with the independent experimental findings by White & Saric (2003), see also the review by Saric, Reed & White (2003).

The entirety of this work resulted in a thorough understanding of the transition process initiated by saturated steady crossflow vortices. In physical space, strong co-rotating vortices are formed with their axes oriented approximately along the outer streamline. Upon downstream vortex saturation, the mean flow is deformed resulting in the formation of strong shear layers, which are connected to local wall-normal and crosswise inflectional mean profiles $u_s(y)$ and $u_s(z)$. They trigger a convective high-frequency secondary instability with explosive spatial growth of unsteady modes. The frequency of the most amplified secondary mode is about one order of magnitude higher than the frequency of the most amplified primary CF mode. (In DNS, unsteady/background disturbances have to be added to the steady flow field.) These instabilities are localized in physical space, i.e. they move focused along the primary vortical structure, and appear mostly in the low-momentum upwelling region, where especially the spanwise gradients in the meanflow become extreme. The growth of these secondary instabilities is connected to the appearance of secondary finger-vortices twining around the crossflow vortices from their upward moving side. We observed final breakdown by tertiary vortices in between the secondary finger vortices.

Principally, three different classes of secondary instability mode were identified: (i) The high-frequency 'mode I' or 'z' mode, induced by the minimum of the spanwise gradient of the streamwise velocity component; this mode seems to be most important (see Wassermann & Kloker 2002; White & Saric 2003); (ii) the high-frequency 'mode II' or 'y' mode, induced by the local maximum of the wall-normal gradient, and (iii) the low-frequency 'mode III', most probably linked to the maximum of the spanwise gradient. The modes exhibit their amplitude maxima in the respective regions of the deformed three-dimensional mean flow, i.e. the most amplified 'z' mode is located at the updraft crossflow vortex side, and the 'y' mode on top of the vortex. The weaker amplified mode-III class is found under the vortex close to the wall.

On the other hand, investigations dealing with transition scenarios characterized by the superposition of steady and unsteady primary disturbances have less conclusive

findings. The basic effect of the interaction on the mode growth was found relatively early in experiments and computations. Malik *et al.* (1994), for example, studied the linear and nonlinear crossflow disturbances as well as the interaction between steady and travelling modes in swept Hiemenz flow solving the PSE. They found that 'when the initial amplitude of the stationary vortex is larger than the travelling mode, the stationary vortex dominates most of the downstream development. When the two modes have the same initial amplitude, the travelling mode dominates the downstream development owing to its higher growth rate.' These results were confirmed by other investigations, see, e.g. the DNS work of Wintergerste & Kleiser (1996, 1997), Bonfigli & Kloker (1999, 2000), and the investigations of Huai, Joslin & Piomelli (1999) using large-eddy simulation. As for the later transition stages, a common conclusion is: whenever a strong travelling CF vortex is present and interacts with a still significant steady CF vortex (of at least 10% u_s-disturbance amplitude), the three-dimensional steady flow deformation is distinctly weaker, but transition can set in comparably early. The DNS work gives some indication that in this case the nonlinear interaction of the primary steady and travelling modes/vortices generates vortical interaction structures that lead the transitional process before some kind of known secondary instabilities come into play. Moreover, the amplitude ratio of travelling to steady mode and the amplitude of possibly provided additional background disturbances have a major influence on the process. We point out that, at clean conditions, an unsteady pure single crossflow wave cannot lead to transition (in a convectively unstable manner) because it generates only non-zero diagonal elements in the frequency-spanwise wavenumber space, and the necessary spectrum-filling modes have to be added.

In the experiments of Lerche (1996, 1997) and Bippes (1999) two different cases were distinguished with controlled unsteady-wave input. First, the case $(0, 1) + (1, 1)$, characterized by both a saturated steady and unsteady crossflow mode attaining an amplitude of about 10% each, and secondly, the case $(1, 1)$ with only the unsteady mode $(1, 1)$ forced resulting in a saturation amplitude of 10% for the unsteady wave and a saturation amplitude of only 2% for the experimentally unavoidable steady vortex mode. Both scenarios reveal an enormous complexity for the disturbance development and initiation of final breakdown. An indication was found that in the wave dominated case $(1, 1)$ a co-travelling secondary instability exists, with somewhat similar appearance to the mechanism found in case $(0, 1) + (1, 1)$ (see figure 1, taken from Lerche's dissertation 1997). The isocontours of the wall-normal gradient and the second time derivative of the streamwise velocity component in a flow-field crosscut over time give an indication of higher-frequency activity around the gradient tubes. Lerche could not further analyse the mechanism with the experimental data since storage of the full three-dimensional unsteady flow field would have been necessary. In his concluding review Bippes focused on the wall-normal gradients of the local instantaneous flow. Note also that the steady-vortex amplitude is not negligible in this case.

Growth rates of a secondary instability induced by travelling primary crossflow waves on a swept cylinder have been calculated by Malik, Li & Chang (1996), using secondary instability analysis in a reference frame moving with the spanwise phase speed of the primary wave. They found the rates twice as high as in the case with steady primary disturbances, and at somewhat lower frequencies, but did not further analyse this finding because in the corresponding experiment the frequency of the secondary instability connected to the steady primary vortices dominated.

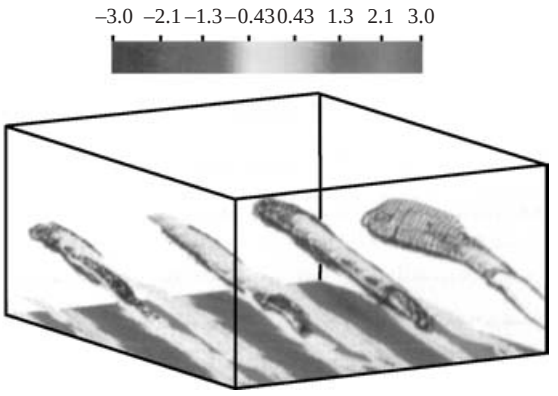

FIGURE 1. Crossflow-wave induced secondary instability (figure 76b from Lerche 1997, experiment at DLR Göttingen). Shown are isocontours of the wall-normal gradient (also at the wall) of the streamwise disturbance velocity component u_s induced by the travelling primary vortices (tubes); the dark clouds around the tubes mark high values of the second time derivative of u_s. Spanwise cut over a fundamental time period.

Seemingly of academic interest at first, we find the investigation of purely travelling primary vortices a prerequisite for further proceeding in the detailed understanding of the transition mechanisms active in practically relevant cases with unsteady crossflow vortices involved. In all experimental and DNS investigations dealing with unsteady crossflow modes known so far, including our own work, a timewise/spanwise or streamwise/spanwise Fourier decomposition of the disturbance flow has been applied in a fixed frame of reference. This indeed prohibited an insightful analysis of the data gained. Thus, we have simulated the transition process initiated by a pure single crossflow wave superposed by small-amplitude background disturbances at its saturation by spatial DNS, and employed a refined analysis method upon moving spanwise with the wave to tackle the following issues:

(i) documentation of the unsteady saturated primary state;
(ii) identification of possibly existing relevant secondary instability modes;
(iii) identification and clarification of the transition mechanism;
(iv) visualization of flow structures throughout the laminar breakdown;
(v) comparison to steady crossflow-vortex induced transition: similarities and differences.

The structure of the paper is as follows: In § 2, a brief summary of the numerical method is given. In § 3, the considered laminar base flow is presented, and in § 4, its primary stability properties are analysed. In § 5, the laminar breakdown initiated by the saturated crossflow wave is investigated in detail. In § 5.1, the saturated primary state is documented, and in § 5.2, the secondary instability mechanism triggering transition is identified and analysed.

2. Numerical method

The numerical method for spatial DNS is based on a vorticity-velocity formulation. All variables are non-dimensionalized by the reference length $\bar{L} = 0.05\,\mathrm{m}$, the chordwise free-stream velocity $\bar{U}_\infty = 30\,\mathrm{m\,s^{-1}}$ and the Reynolds number $Re = \bar{U}_\infty \bar{L}/\bar{\nu} = 100\,000$, where the overbar denotes dimensional variables and $\bar{\nu}$ is the kinematic viscosity.

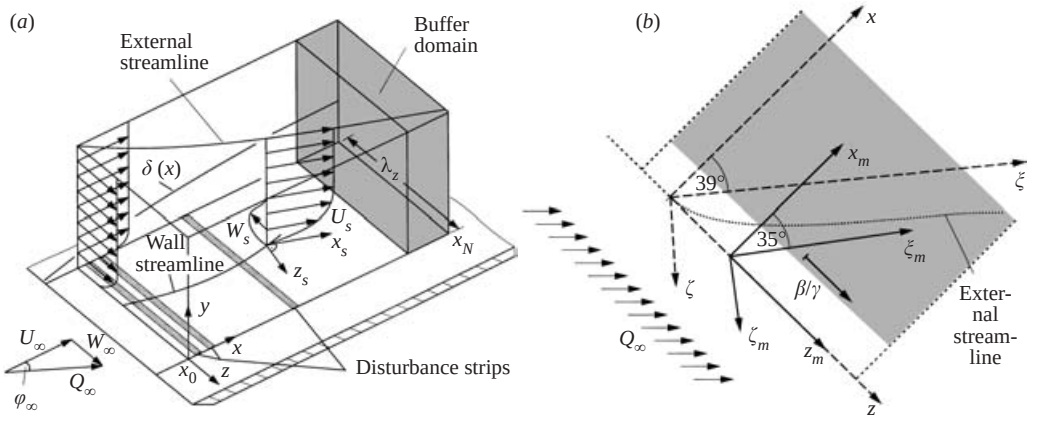

FIGURE 2. (*a*) Integration box. (*b*) Top view of the swept flat plate with the body-fixed chordwise coordinate system (x, z), the body-fixed streamwise system (ξ, ζ) (rotated by $\psi = 39°$), the moving chordwise system (x_m, z_m) with $z_m = z - \beta_1/\gamma_1 t$, and the moving streamwise system (ξ_m, ζ_m) (rotated by $\psi_m = 35°$).

We have the vectors of vorticity $\boldsymbol{\omega} = \{\omega_x, \omega_y, \omega_z\}^T$ and velocity $\boldsymbol{u} = \{u, v, w\}^T$, with the first component in the chordwise (x-), the second component in the wall-normal (y-) and the third component in the spanwise (z-) direction. The vorticity components are defined as

$$\omega_x = \frac{\partial v}{\partial z} - \frac{\partial w}{\partial y}, \quad \omega_y = \frac{\partial w}{\partial x} - \frac{\partial u}{\partial z}, \quad \omega_z = \frac{\partial u}{\partial y} - \frac{\partial v}{\partial x}. \tag{2.1}$$

We use a disturbance formulation keeping the full equation set, in order to ease formulation of boundary conditions. For the infinite swept conditions, each flow variable is split into the steady laminar base flow part with $\partial/\partial z \equiv 0$ (index B) and the unsteady three-dimensional disturbance flow part (denoted by a prime):

$$f(x, y, z, t) = f_B(x, y) + f'(x, y, z, t) \quad \text{with} \quad f \in \{u, v, w, \omega_x, \omega_y, \omega_z\}. \tag{2.2}$$

Note that for nonlinear disturbances, the time mean $\langle f' \rangle \neq 0$, of course. The simulation is carried out in a rectangular integration domain (figure 2). Owing to the disturbance formulation, the simulation splits up into two steps. First, the steady base flow is calculated; subsequently, defined disturbances are introduced in disturbance strips at the wall and the disturbance flow is calculated. All base flow quantities are independent of the spanwise coordinate z, but there is a velocity component w_B in the spanwise direction. For the calculation of the disturbance quantities, the assumption of infinite span yields periodic boundary conditions in the spanwise direction. Thus, the numerical method uses a complex Fourier spectral representation in the spanwise direction to calculate the non-symmetric three-dimensional flow (with periodicity $\lambda_z = 2\pi/\gamma_1$). In the x- and y-directions, a finite-difference (FD) discretization is used, based on a blockwise equidistant rectangular grid with a special wall zone, where the step size Δy is halved. Principally, sixth-order compact FDs are used. The nonlinear terms in the vorticity transport equations are computed pseudospectrally and their x-derivatives are differenced with a special split-type method with inherent damping; the time integration is done by a 4-step fourth-order Runge–Kutta method. For a detailed description of the numerical method see Kloker (1998), Bonfigli & Kloker (1999) and Wassermann & Kloker (2002).

Defined disturbances are introduced in the laminar flow field in several disturbance strips at the wall where the disturbances are enforced with momentum input, but no net mass flow:

$$v'(x,0,z,t) = f_v(x)\left(\sum_{k=1}^{K} 2A_{0,k}\cos(k\gamma_1 z + \Theta_{0,k}) + \sum_{h=1}^{H}\sum_{k=-K}^{K} 2A_{h,k}\cos(k\gamma_1 z - h\beta_1 t + \Theta_{h,k})\right). \quad (2.3)$$

The first sum represents a steady part that is only used for a reference case for comparison. f_v is a piecewise-defined symmetric fourth-order parabola ($-3\tau^4+4\tau^3$ for $0 \leqslant \tau < 1$, and $-3(2-\tau)^4+4(2-\tau)^3$ for $1 \leqslant \tau \leqslant 2$, $[0,2] \mapsto [x_j - 0.5\Delta x_s, x_j + 0.5\Delta x_s]$; it has vanishing first and second derivatives at the respective ends of the strips; γ_1 is the fundamental spanwise wavenumber.

For the analysis of the unsteady three-dimensional flow data, different coordinate systems are used (see figure 2(*b*)). First, we have the body-fixed chordwise system (x, y, z). Secondly, we have the body-fixed streamwise system (ξ, y, ζ) that is rotated with respect to the (x, y, z)-system by a fixed angle of 39° to follow the only slightly changing direction of the outer streamline. The other systems, the wave-fixed chordwise system (x_m, y, z_m) and the wave-fixed streamwise system (ξ_m, y, ζ_m), represent Galilean-transformed systems and are moving (index m) in the positive z-direction at constant speed c_z to follow the movement of the dominating primary crossflow wave; $c_z = \beta_1/\gamma_1 = h\beta_1/(k\gamma_1)$ for $h = k$, where β_1 is the fundamental frequency:

$$z_m = z - c_z t = z - \beta_1/\gamma_1 t. \quad (2.4)$$

Note that a single crossflow wave, denoted as mode (1, 1) where the numbers give h, k, respectively, nonlinearly generates only modes with $h = k$ like (2, 2), (3, 3), etc., that all have the same phase speed c_z. The moving streamwise system is rotated by a fixed angle of 35° to account for the different direction of the outer streamline in the moving system.

2.1. *Code validation*

The numerical method is well tested; for the investigations presented here, we have compared the quasilinear development of a small-amplitude unsteady CF wave with DNS-results of Spalart, Crouch & Ng (1994). The chordwise amplitude developments shown in figure 3 coincide as well as the results for steady crossflow modes in former calculations (Wassermann & Kloker 2002). Even in the transient region just downstream the excitation of the disturbance, the amplitude developments coincide, although Spalart *et al.* apply a body force inside the boundary layer, whereas forcing at the wall by the wall-normal velocity is used in our studies.

2.2. *Numerical parameters*

For the following simulations, the uniform blockwise equidistant grid typically contained 2106 × 257 points in the (x, y)-directions (with $\Delta x = 0.0017952$, $\Delta y = 0.000278$). In the spanwise direction first $K = 16$ spectral modes, corresponding to $\gamma_{\max} = 1440$, are used. For the first 33 points in the wall-normal direction $\Delta y_{wz} = \frac{1}{2}\Delta y$. The number of time steps per fundamental disturbance period $\beta_1 = 2\pi \bar{f}\bar{L}/\bar{U}_\infty = 14$ was 1200. In former investigations, it has been shown that even $\gamma_{\max}$ only equal to eight times the wavenumber of the dominating primary mode is fine enough to capture

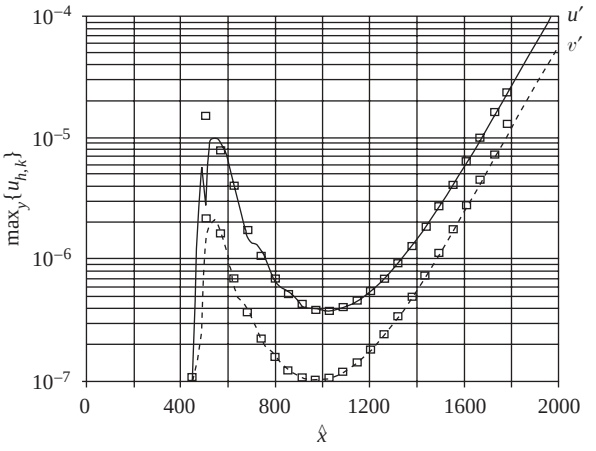

FIGURE 3. Comparison of the chordwise amplitude development with results of Spalart *et al.* (1994). The background plot shows the $u'_{(1,1)}$ and $v'_{(1,1)}$ amplitude development for an unsteady mode with $\beta = 16$, $\gamma = 21$, as scanned from their paper, figure 4. Our DNS results are marked by the symbols. Here $\hat{x} = 400x$; $\gamma = \bar{\gamma}\bar{L}$. The u'-amplitude curve is fit near $\hat{x} \approx 1000$, with the ratio u'/v' untouched.

correctly the onset of secondary instability and its initial quasilinear growth. For the calculation of the later stages of transition the numerical resolution is significantly refined. Here, a grid with $K_f = 32$, $\Delta x_f = \frac{1}{2}\Delta x$, $\Delta y_f = \frac{2}{3}\Delta y$ and $\Delta t_f = \frac{1}{2}\Delta t$ is used.

The problem has been run on the NEC SX-5 (16 vector-processors, 32 GB RAM) of the high-performance computing centre at Stuttgart (HLRS). A calculation takes about 2.2 µs per gridpoint and full time step on a single processor. The performance is about 2 GFLOPS per CPU, representing 50% of the theoretical peak performance.

3. Laminar base flow

The base flow is designed to resemble the flow in the upper front region of a swept wing and is the same as used in our previous study (Wassermann & Kloker 2002). The streamwise edge velocity is adopted from Spalart, Crouch & Ng (1994) and defined analytically by

$$u_{p0}(x) = \frac{3}{2\pi}\left(\arctan\left(\frac{x-a}{b}\right) + \arctan\left(\frac{x+a}{b}\right)\right) - cx \tag{3.1}$$

with

$$a = 0.2611, \quad b = 0.41015, \quad c = 0.056.$$

The integration domain starts at $x_0 = 0.25$ close to the leading edge (local Hartree $\beta_H(x_0) = 0.99$) and extends for the following investigations up to $x_N = 4.03$. The sweep angle is $\varphi_\infty = 45°$ and the local angle of the external streamline varies from $\varphi_e(x_0) = 68.1°$ to the minimum value of $\varphi_e = 39.7°$ at $x = 2.65$ and $\varphi_e(x_N) = 40.3°$ (figure 4). The Reynolds number based on the chordwise displacement thickness δ_1 rises from $Re_{\delta 1}(x_0) = 67$ to $Re_{\delta 1}(x_N) = 1180$ and the displacement thickness increases by a factor of six within the domain. The crossflow amplitude $\tilde{w}_{s,B} = w_{s,B}/u_{s,B,e}$ decreases from 13% to 4% in the relevant region (see figure 5); the crossflow Reynolds-number range is $60 \leqslant Re_{CF} \leqslant 130$ ($Re_{CF} = w_{s,B,max}\bar{U}_\infty \bar{y}_{10}/\bar{\nu}$, $\bar{y}_{10}$: far-wall y-position where $w_{s,B} = 0.1 \times w_{s,B,max}$). The maximum value is at $x = 1.75$.

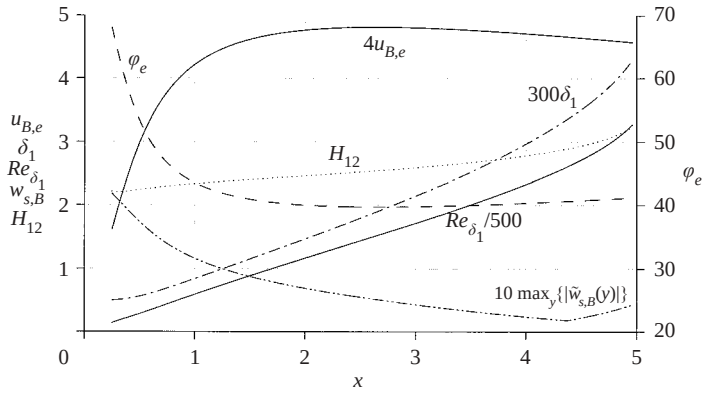

FIGURE 4. Base-flow parameters in the plate-fixed coordinate system.

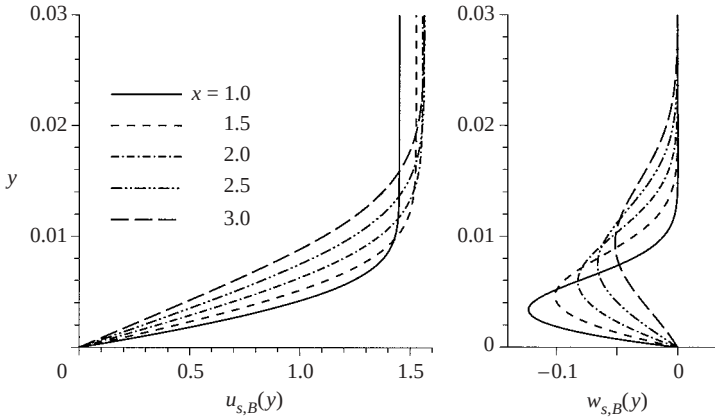

FIGURE 5. Meanflow and crossflow profiles at various downstream positions.

4. Primary instability properties

4.1. *Linear stability theory*

The laminar baseflow has been analysed in detail by means of spatial linear stability theory (LST) to obtain an overview of relevant instability modes. Figure 6 shows the stability diagram as a function of spanwise wavenumber γ and frequency β at $x = 1.0$. This position is just downstream of the disturbance excitation in the DNS discussed below. Here, the typical stability properties for dominating crossflow instability can be identified with amplified steady disturbances, weakly amplified waves travelling with the crossflow, and the strongest amplification for waves travelling against the crossflow to the right ($\beta \approx 14, \gamma \approx 110$). For $\beta = 14$, the integrally most amplified frequency up to $x = 2.0$, the stability diagram is plotted in figure 7 as a function of chordwise coordinate and spanwise wavenumber. Here, the persistent stronger amplification for the right-travelling waves is clear-cut, and the shift of the maximum amplification to lower γ values for larger x is visible. Furthermore, $\gamma = 90$ can be identified as one of the most amplified wavenumbers.

As a result of the stability analysis, the fundamental values $\gamma_1 = 90\,(= \bar{\gamma}_1 \bar{L})$ and $\beta_1 = 14.0$ have been chosen for the subsequent DNS. Compared to the computational raster used in former investigations for steady-vortex induced transition (see Wassermann

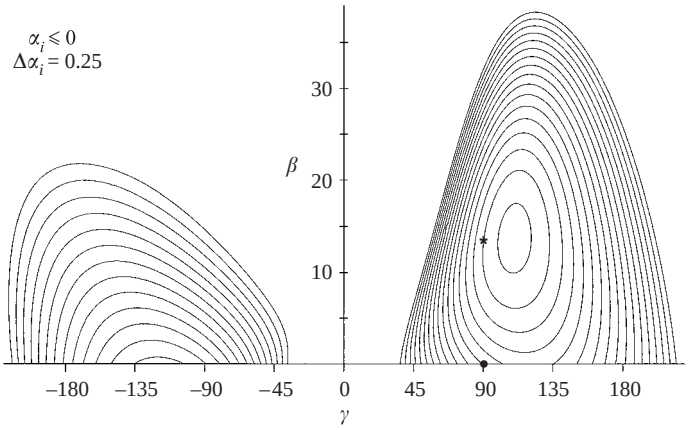

FIGURE 6. Stability diagram from LST at the downstream position $x = 1.0$; $\alpha_i = \bar{\alpha}_i \bar{L} = -1/A \times \mathrm{d}A/\mathrm{d}x$: spatial amplification rate. The modes considered in the DNS later on are marked by the symbols: ★, case WAVE, $\beta = 14, \gamma = 90$; ●, case VORTEX, $\beta = 0, \gamma = 90$.

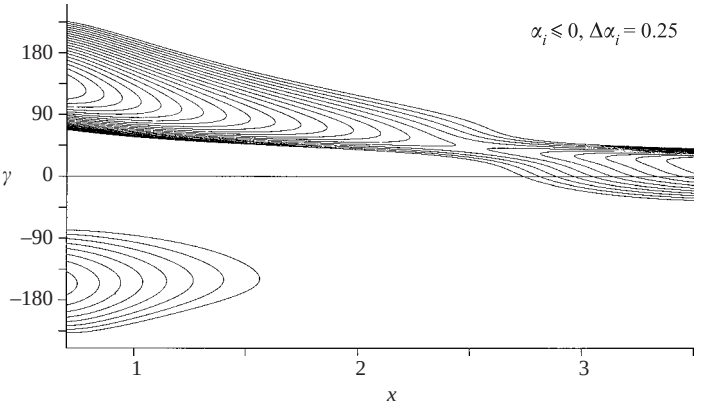

FIGURE 7. Stability diagram from LST for unsteady modes with frequency $\beta = 14.0$.

& Kloker 2002), γ_1 is doubled, and thus the mode notation does not compare. The discrete waves are presented in the frequency-spanwise wavenumber spectrum (h, k), so the mode (h, k) denotes a mode with the spanwise wavenumber $k\gamma_1$ and a frequency that is h times the fundamental frequency β_1.

In figure 6, the primary crossflow modes considered in the framework of this paper are marked by symbols. In case WAVE a single right-travelling wave is considered, whereas in case VORTEX, the steady reference case, a single crossflow vortex mode is forced as primary disturbance.

4.2. *Direct numerical simulation*

In a basic simulation (case LINEAR), the quasilinear development of the steady mode $(0, 1)$ and the unsteady mode $(1, 1)$ has been simulated. The disturbances are introduced at $x = 0.68$ with an amplitude of $A_{(h,k)} = 1.0 \times 10^{-6}$ each. In figure 8, the $(t\text{-}z)$-modal amplitude development clearly shows the mode $(1, 1)$ to be the stronger amplified mode. The steady mode $(0, 1)$ is amplified more continuously resulting in an integral amplification comparable to mode $(1, 1)$. Nevertheless, the amplitude at $x = 3.5$ is only about a fifth the amplitude of mode $(1, 1)$, since the effective initial

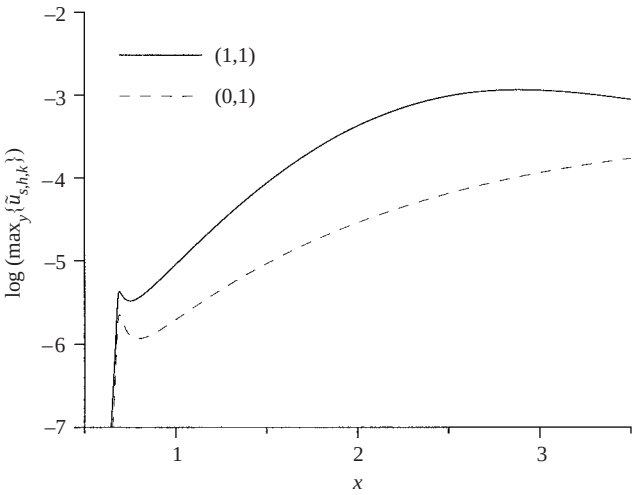

FIGURE 8. Quasilinear downstream (t-z)-modal amplitude development of the crossflow modes (1, 1) and (0, 1) in case LINEAR; $\tilde{u}_{s,h,k}$-maximum over y, $\tilde{u}_s = u_s/u_{s,B,e}$.

amplitude at growth onset is by a factor of about three less. The length of the disturbance strip is $14\Delta x$, corresponding to $0.17\times\lambda_{x,(1,1)}$ and $0.29\times\lambda_{x,(0,1)}$, respectively, where λ_x is the respective chordwise wavelength. The DNS growth rates are somewhat higher throughout the integration domain than predicted by LST.

5. Saturation, secondary instability, and breakdown

The following investigations focus on the nonlinear saturation and secondary instability of an unsteady crossflow mode, and on the final laminar breakdown. The results are compared to a steady-crossflow-vortex dominated scenario considered in former investigations (case VORTEX, which is case 3 in Wassermann & Kloker 2002), to work out similarities and differences. In this reference case, the steady mode (0, 1) has been excited as primary disturbance, and superposed by periodic background pulses resulting in a classical crossflow-vortex induced transition scenario with strongly amplified secondary instabilities triggering the laminar breakdown.

5.1. *Nonlinear saturation of a single unsteady crossflow wave*

For the calculation of a nonlinear, saturated crossflow-wave scenario the crossflow mode (1, 1) is introduced at $x = 0.68$ with an amplitude of $A_{(1,1)} = 5.0 \times 10^{-3}$ in case WAVE. By turning on the disturbance, a moving disturbance front is generated. As this disturbance front is convected downstream, the flow field settles slowly to an unsteady, strictly periodic saturated state. The nonlinearly generated higher harmonics (modes (2, 2), (3, 3) etc.) of the forced mode are the only spectral modes of measurable amplitude in addition to the (0, 0) mode. The superposition of these modes represents the saturated unsteady primary state. Note that these modes travel in the spanwise direction at the same speed β_1/γ_1. In the clean-condition simulation, the off-diagonal elements of the disturbance spectrum in the (h, k)-plane have vanishing amplitudes, and consequently, laminar breakdown does not occur. This, in fact, indicates that no absolute instability with timewise growing disturbances exists.

The (t-z)-modal amplitude development in figure 9(a) shows that the forced disturbance mode is strongly amplified by primary instability first. Directly after

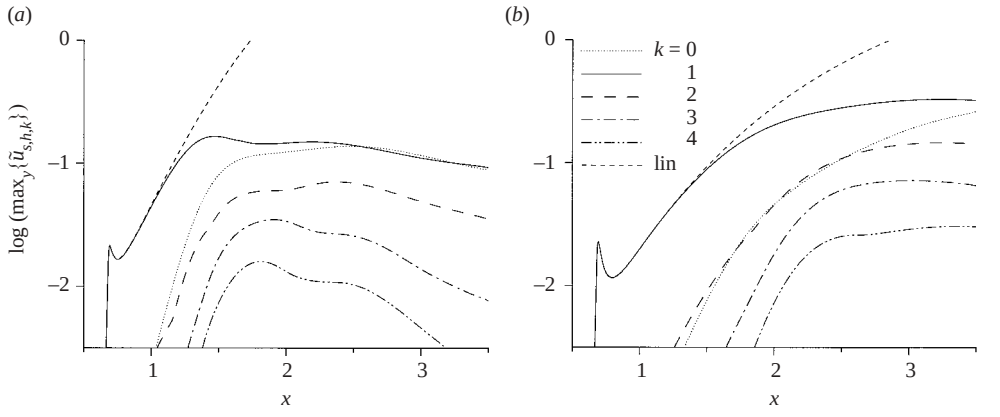

FIGURE 9. Downstream (t-z)-modal amplitude development ($\tilde{u}_{s,h,k}$-maximum over y) in case WAVE (modes (k,k), left) and case VORTEX (modes $(0,k)$, right). The short-dashed line indicates the quasilinear amplification of the forced modes.

excitation, the amplitude growth perfectly coincides with the quasilinear development (case LINEAR), before the mode starts to saturate (saturation at $x \approx 1.4$) and finally slightly goes down in amplitude. We note that the decay of $(1,1)$ downstream of $x = 2.4$ in figure 9(a) is due to changing baseflow properties, as a simulation with a constant Hartree-parameter baseflow only shows the slight amplitude drop after first saturation, followed by a further slight increase over the first saturation level. (This behaviour is consistent with observations of Koch *et al.* 2000, see their figure 10b). For comparison, figure 9(b) shows the amplitude development in the reference case VORTEX with steady primary disturbance mode. Obviously, the steady modes are less sensitive to the changing baseflow properties.

Accordingly, in case WAVE, one travelling vortex per spanwise wavelength evolves with clockwise rotation when looking downstream (see figure 10). The vortex axes are aligned with an angle of about 9° to the inviscid streamline in the fixed system, and the vortices are travelling in the positive z-direction at constant speed β_1/γ_1. Upon passing by, the vortices instantaneously transport slow fluid from the near-wall region up into faster regions resulting in an unsteady deformation of the meanflow profiles $u_s(y)$ and $u_s(z)$, with relatively large y-gradients. In figure 11, the time-averaged meanflow profiles at various crosswise positions in the fixed system $\langle\tilde{u}_s(y)\rangle$ and in the moving system $\langle\tilde{u}_{s,m}(y)\rangle$ are shown. Here, it becomes obvious that only the consideration of the moving system yields expressive results. In the fixed system, the time-averaged mean flow profiles do not show any spanwise variation, known from steady-crossflow-vortex dominated regimes, because the vortex movement is averaged out. Nevertheless, those profiles are often employed as a criterion for secondary instability even if unsteady waves are involved (see, e.g. Bippes 1999). Only the two-dimensional distortion of the meanflow, mode (0, 0), adds to the baseflow profile. (The partial thickening of the curve seen here is caused by the x-development of mode (0, 0) since x varies with constant ξ). On the other hand, in the system moving with the vortex, a strong crosswise variation can be identified, not unlike the variation in case VORTEX in the fixed system.

The figures 12 and 13 show the deformed flow field in case WAVE; in figure 14 case VORTEX is shown with identical scaling. The detailed comparison reveals several significant differences in the three-dimensional deformation of the flow. In figure 12,

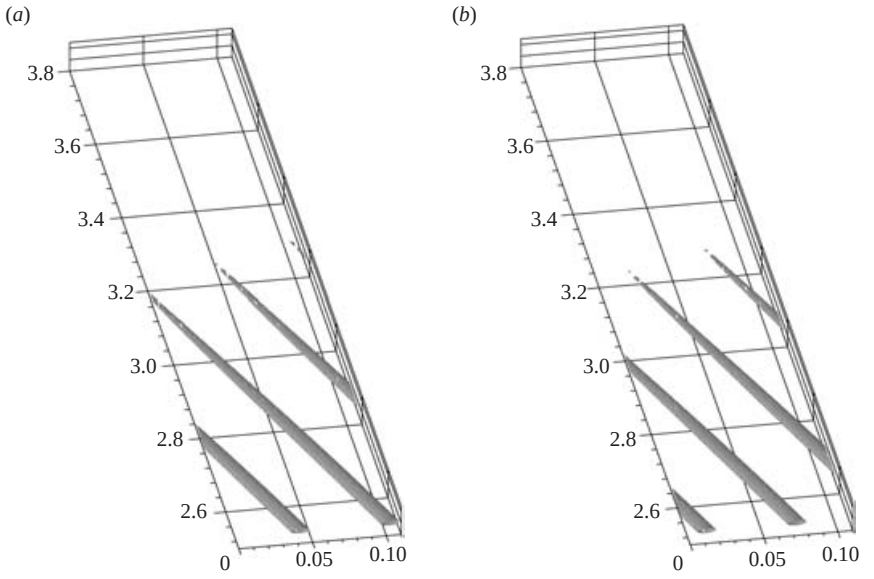

FIGURE 10. Visualization of vortical structures in the instantaneous flow fields for case WAVE by λ_2-isosurfaces, $\lambda_2 = -50$. Approximately two spanwise wavelengths are shown; note the compression of the ξ-axis. (*a*) $t/T = 0$, (*b*) $t/T = 0.5$.

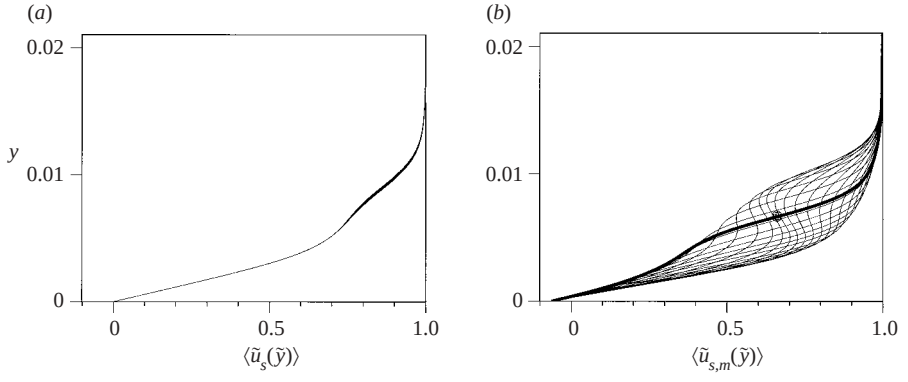

FIGURE 11. Mean flow profiles at equidistant crosswise positions for case WAVE. (*a*) Fixed streamwise system, $\xi = 2.0$. (*b*) Moving streamwise system, $\xi_m = 2.0$. The profile for $\zeta_m = 0.068$ is emphasized and the dot marks the wall-normal position of the maximal amplitude of the most amplified secondary instability mode.

the instantaneous flow deformation of case WAVE is shown in the fixed streamwise coordinate system; figure 13(*a*) shows it in the moving streamwise system. Apart from an arbitrary phase shift, the figures mainly collapse; the small differences are caused by the slightly different velocity and axes directions. Thus, for the following comparison with the steady reference case the presentation in the moving system (figure 13) is used, in which the travelling wave appears as a steady one.

Compared to case VORTEX, in case WAVE all structures are situated much closer to the wall. The centre of the travelling vortex is situated at half the boundary layer thickness δ, and the region of noticeable $\tilde{u}'_s$ extends as far as 0.9δ; the corresponding

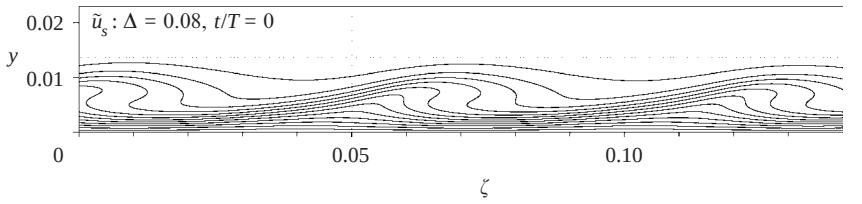

FIGURE 12. Instantaneous u_s-isolines in a crosscut in the fixed streamwise system at $\xi = 2.0$ for case WAVE in the saturation state. To scale.

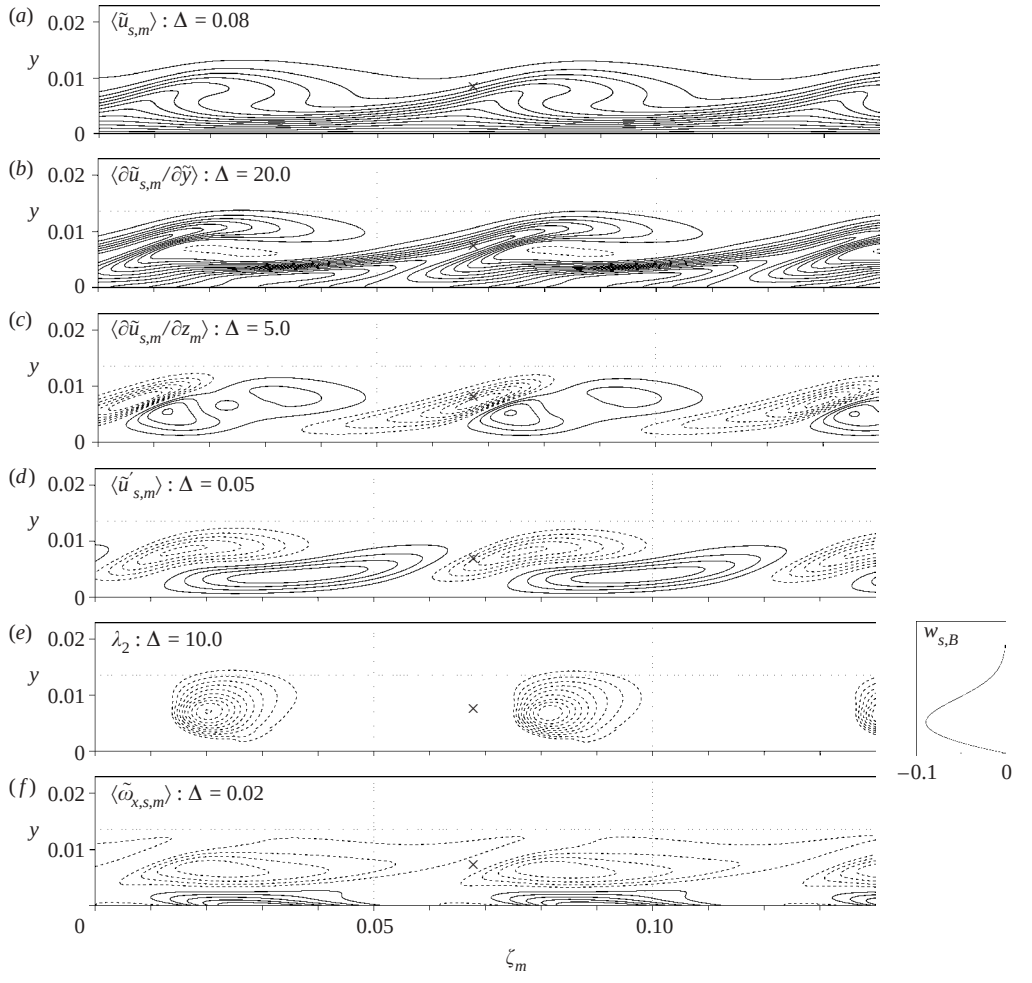

FIGURE 13. Flow field crosscuts for case WAVE (nonlinearly saturated crossflow wave) in the moving streamwise system at $\xi_m = 2.0$: (*a*) deformed mean flow; (*b*), (*c*) *y*- and z_m-gradient of the deformed meanflow; (*d*) deformation of the mean flow; (*e*) λ_2 isolines; (*f*) vorticity component in mean-flow direction. Negative isolines are dashed, the zero line is not shown. To scale. The dotted horizontal line markes the laminar boundary-layer thickness at $\zeta_m = 0$. This quantity varies only by 2% over the ζ_m-range shown here. The insert on the right-hand side shows the crossflow profile $w_{s,B} = w_{s,B,m} + \beta_1/\gamma_1$ at $\xi_m = 2.0$, $\zeta_m = 0$. The cross marks the position also marked in figure 19(*c*).

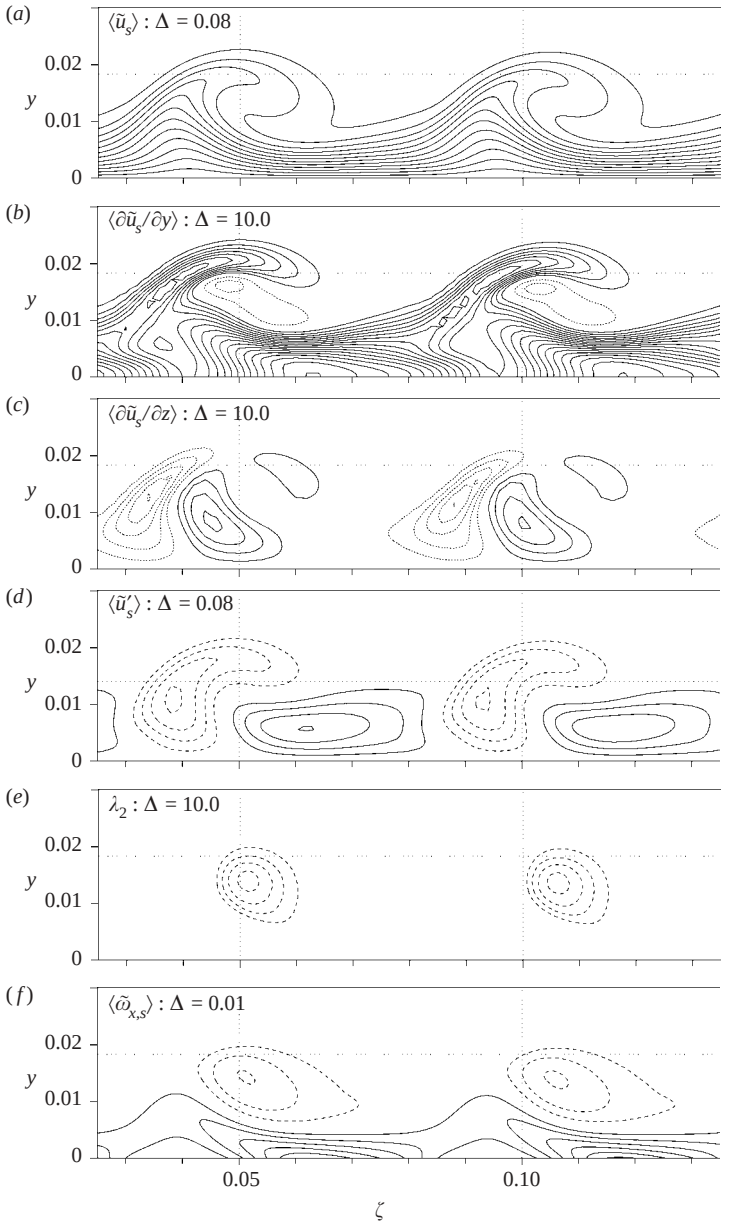

FIGURE 14. Same as figure 13 but for the reference case VORTEX at $\xi = 3.2$ (from Wassermann & Kloker 2002).

values for case VORTEX are $0.8\,\delta$ and $1.5\,\delta$, respectively (figures 13*d*, *e*, 14*d*, *e*). Owing to the travelling primary disturbance, the structures are somewhat stretched in the spanwise direction, even in the moving system. The regions of local acceleration and deceleration (figure 13*d*) overlap, whereas a clearer spanwise separation is present in case VORTEX (figure 14*d*). The most pronounced shear layer is relatively flat in the unsteady case with an angle of only about 16° whereas it is 40° in the steady case (figure 14*a–c*). Thus, the *y*-gradients are much larger than the *z*-gradients, with the ratio 4.3:1 versus 1.2:1.

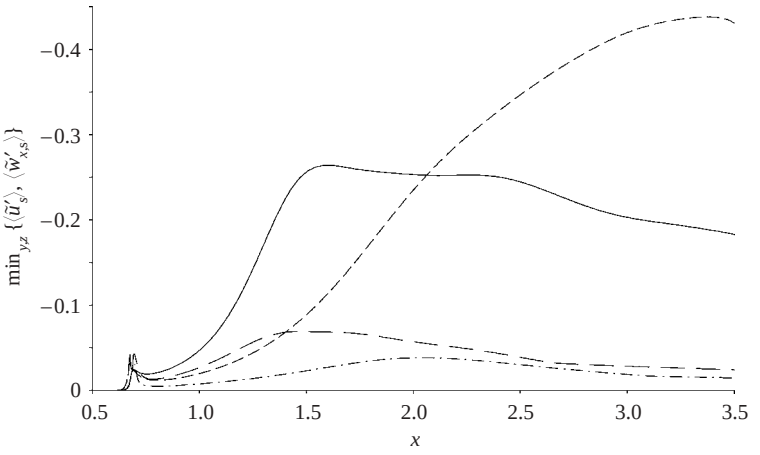

FIGURE 15. Downstream development of the maximal (over y and z) deceleration of the mean flow and the modulus of the streamwise vorticity (maximal clockwise rotation) in the cases WAVE and VORTEX. ——, WAVE: $\min\{\langle\tilde{u}'_{s,m}\rangle\}$; — — —, WAVE: $\min\{\langle\tilde{w}'_{x,s,m}\rangle\}$; – – –, VORTEX: $\min\{\langle\tilde{u}'_s\rangle\}$; – · –, VORTEX: $\min\{\langle\tilde{w}'_{x,s}\rangle\}$.

The maximum local deceleration of the mean flow $\langle\tilde{u}'_{s,m}\rangle$ in the unsteady case WAVE does not surpass the threshold level that we found for the onset of secondary instability in case VORTEX ($\langle\tilde{u}'_s\rangle \leqslant -0.3$), although the maximum local streamwise vorticity $\omega_{x,s,m}$ is significantly larger than in the steady case (figure 15). We observe that in case WAVE, the deceleration amplitude follows the maximum local strength of the streamwise vorticity component, whereas in case VORTEX, the streamwise gradient of the deceleration does so. In the steady case, the lift-up of slow fluid from the near-wall region to the outer part of the boundary layer induced by the streamwise vortices is much more pronounced owing to the persistent positive wall-normal velocity disturbance at fixed locations. This leads to an integrated effect along the streamwise direction since the vortices are steady with their axes aligned along the potential streamline. For the travelling vortices whose axes are tilted with respect to the streamwise direction, such an integral effect cannot occur.

5.2. *Secondary instability and laminar breakdown initiated by the single unsteady crossflow wave*

In the WAVE scenario discussed so far, the flow field finally settles to an unsteady, saturated, strictly periodic state without laminar breakdown. Naturally, transition to turbulence can only be caused by unsteady disturbances filling the frequency–spanwise-wavenumber spectrum. To this end, periodically pulsed low-amplitude disturbances have been superimposed in case WAVE + B to model the natural disturbance background. The periodic background pulse consists of superposed, in-phase harmonic waves with discrete frequencies from $\beta = 14$ up to $\beta = 350$ with $\Delta\beta = 14$, for $k = \pm 1$, with $A_{(h,\pm 1)} = 5.0\times10^{-5}$ and $\Theta_{h,k} = 0$ for each component (see equation (2.3)), and has been excited at $x_3 = 1.25$, just upstream of the saturation point of the primary disturbance. It is only given for the spectral component $k = \pm 1$, since the large-amplitude mode (1, 1) and its higher harmonics generate the other background spectral components at once.

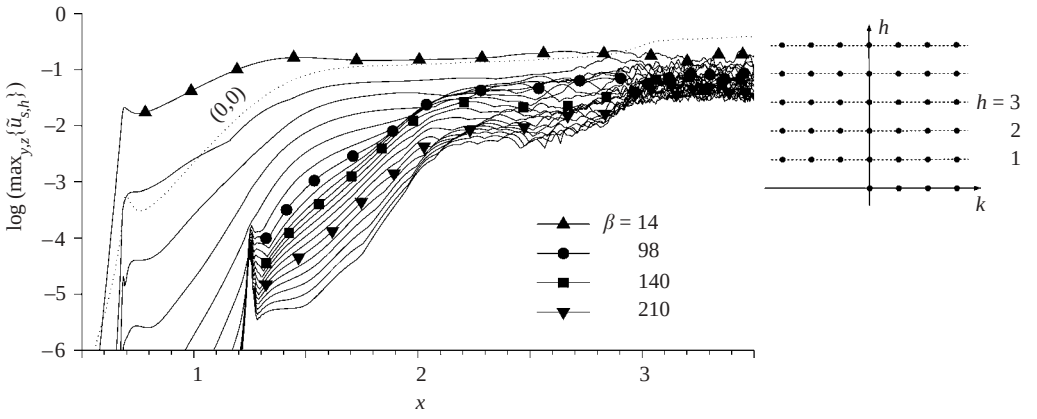

FIGURE 16. Downstream t-modal amplitude development for case WAVE + B in the fixed system: single crossflow wave plus periodic background pulses. Frequencies from $\beta = 14$ to $\beta = 238$, $\Delta\beta = 14$, are shown. The curve denoted by (0, 0) represents the two-dimensional part of the mean flow distortion. The sketch to the right-hand side illustrates the coherence of (t-z)-modal and t-modal decomposition in the fixed system.

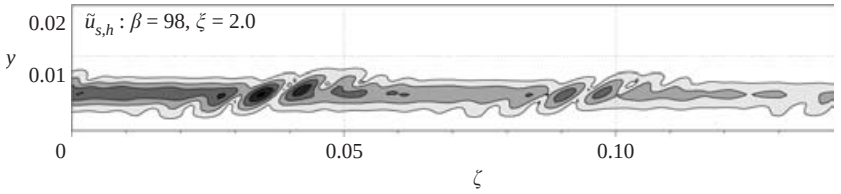

FIGURE 17. Isocontours of normalized $\tilde{u}_{s,h}$-amplitude for case WAVE + B in a crosscut in the fixed streamwise system. Isolines from 0.35 to 0.95 with a 0.2 spacing are shown. The dotted line indicates the laminar boundary-layer edge. To scale.

In investigations of transition scenarios dominated by steady CF vortices, the t-modal representation

$$\tilde{u}'_s(x, y, z, t) = \sum_{h=0}^{H} \tilde{u}_{s,h}(x, y, z) \exp(-\mathrm{i}(h\beta_1 t - \Theta_h(x, y, z))), \tag{5.1}$$

has proved to be a suitable analysis method. It can be recomposed from the classical (t-z)-modal decomposition into modes (h, k) by collecting the modes $(h, k), k = -K, \ldots, K$ for each h. The secondary instabilities triggering transition are clearly characterized by their two-dimensional amplitude distribution $\tilde{u}_{s,h}(y, z)$ in flow-field crosscuts and the downstream development of the amplitude maximum (over y and z) rather than their (β-γ)-spectral content.

In figure 16, the result of such a t-modal analysis is shown for case WAVE + B. After a short transient region, strong amplification can be seen for the high-frequency background disturbances ($\beta = h\beta_1 \approx 140$), whereas the low-frequency background disturbances cannot be identified, since their amplitudes are mainly hidden in the nonlinear higher harmonics of the fundamental wave (modes (h, k) with $h = k$). The amplitude distribution for one frequency in the crosscut in figure 17 shows that the spanwise movement of the events smears this distribution. Thus, it is necessary to isolate all modes (h, h) that just represent the saturated unsteady primary vortex.

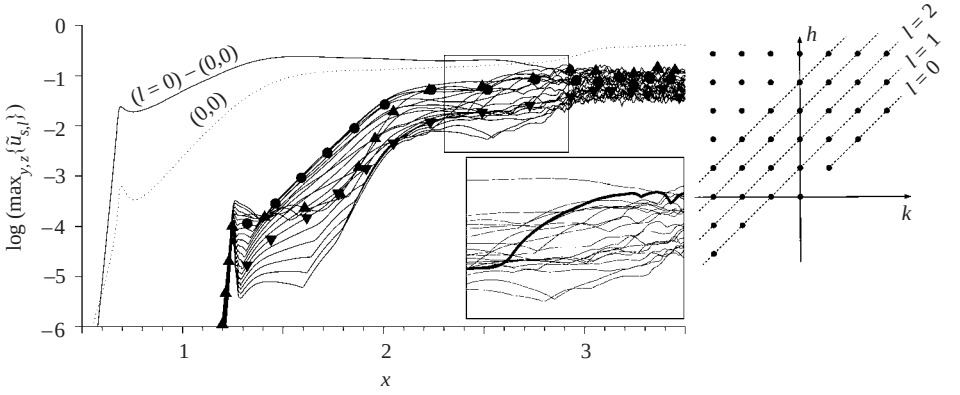

FIGURE 18. Downstream t-modal amplitude development for case WAVE + B in the moving system: single crossflow wave plus periodic background pulses. Frequencies from $\beta_m = 0$ to $\beta_m = 238$, $\Delta\beta_m = 14$, are shown. The curve denoted by $(l = 0) - (0, 0)$ represents the unsteady primary saturated state that is steady ($\beta_m = 0$) in the moving system. ▲, $\beta_m = 14$; ●, 98; ▼, 210. The insert shows a close-up with the frequency $\beta_m = 42$ emphasized. The sketch on the right-hand side illustrates the coherence of (t-z)-modal and t-modal decomposition in the fixed and the moving system, respectively.

An appropriate analysis method for wave dominated scenarios is the t-modal decomposition in the Galilean-transformed system ($z_m = z - \beta_1/\gamma_1 t$):

$$\tilde{u}'_{s,m}(x, y, z_m, t) = \sum_{l=0}^{L} \tilde{u}_{s,l}(x, y, z_m) \exp(-\mathrm{i}(l\beta_1 t - \Theta_l(x, y, z_m))). \tag{5.2}$$

This representation can be recomposed from the classical (t-z)-modal decomposition by summing up the modes $(k + l, k), k = -K, \ldots, K$ for each l, i.e. the modes belonging to the same diagonal as in the sketch in figure 18. Thus, (β-γ)-spectral modes with different frequencies have to be composed. Now, the secondary instability modes are no more characterized by a distinct frequency in physical space as long as the measuring position is steady, as it is for steady primary disturbances. The content of the secondary mode in the frequency space corresponds to its spectral content in spanwise wavenumber space, i.e. each secondary mode causes a multi-frequency time signal at a fixed measuring position. In fact, equation (5.2) removes the Doppler frequency shift felt by a steady observer when looking at the secondary instability modes that travel with the primary wave.

With this analysis method, the secondary instability behaviour becomes transparent. The unsteady primary saturated state is represented by one curve ($l = 0$, i.e. $\beta_m = l\beta_1 = 0$), and the secondary modes can be unambiguously identified, see figure 18. After a short transient region the background disturbances undergo strong amplification, especially the component $\beta_m = 98$, which attains the largest amplitude in this region. This mode grows over the smaller frequency modes, although its effective initial amplitude is smaller. The maximum amplification rate is slightly higher than in the reference case VORTEX + B. For the growth of the low-frequency modes, a significant change can be observed. First, the modes are neutrally stable or even damped, but in the end they grow very fast, clearly nonlinearly generated by the high-frequency modes. Recall that modes l_1 and l_2 generate modes $l_1 \pm l_2$.

Downstream of $x \approx 2.1$, a distinct saturation plateau of the secondary instabilities can be observed. In contrast to steady crossflow-vortex scenarios, here the growth of

the secondary instabilities does not lead directly to laminar breakdown: it takes about 3.5 fundamental streamwise wavelengths from the beginning of secondary saturation to the final breakdown. During this stage, modes around $\beta_m = 42$ distinctly grow and seem to end the transition, see the inset in figure 18.

Before going on with the detailed analysis of the disturbance development, we will discuss the influence of an additional primary subharmonic wave (0.5, 0.5) with about the (1, 1) amplitude at the first disturbance strip. A DNS of this case reveals that (1, 1) is virtually unaltered and that downstream of the saturation of (1, 1) the subharmonic mode surpasses (1, 1) in amplitude for $x > 2.3$. This is reminiscent of subharmonic secondary instability but may, apart from nonlinear interactions, be caused partially by primary instability because (0.5, 0.5) indeed grows primarily stronger than (1, 1) and persistent for $x > 2.3$. In physical space, first two travelling vortices per subharmonic spanwise wavelength are visible according to the grown (1, 1) mode. However, with growing (0.5, 0.5) they do not merge as known from spanwise vortices in free shear flows, but one of them becomes stronger and larger further downstream while the other disappears. The high-frequency secondary instability is observed at the stronger vortex with the same properties as in the case WAVE + B discussed here in detail. The inclusion of subharmonic modes (with multiples of $\beta = 7$) in the background pulse also does not lead to a different evolution. The secondary mode $\beta_m = 7$ behaves very much like $\beta_m = 14$.

Continuing the analysis of case WAVE, isocontours of the $\tilde{u}_{s,l}$-amplitude for $\beta_m = 14$, $\beta_m = 98$ and $\beta_m = 210$ in the crosscut corresponding to figure 13 reveal the origin of the secondary instability (figure 19). For the most amplified instability with $\beta_m = 98$ the location of the largest amplitude – marked by the cross – perfectly coincides with the minimum of the z_m-gradient of the time-averaged streamwise velocity component, see figure 13(*c*), $\zeta \approx 0.068$. Since the y-gradient at this position is about four times larger, it is not so obvious to call this secondary mode a 'z' mode as done in the reference case VORTEX + B. The high-frequency mode ($\beta_m = 210$) is situated somewhat further away from the wall in the top region of the shear layer, and clearly is reminiscent of the 'y' mode found in the former investigation of crossflow-vortex dominated scenarios. The low-frequency mode $\beta_m = 14$ clearly alters its amplitude distribution downstream. In the region of neutral behaviour it is rather distributed (figure 19*a*), whereas it is a distinct localized mode, with a double-maximum appearance, once it strongly grows (figure 19*b*). The mode with $\beta_m = 42$ that seems to end the saturation stage is located at the downdraft vortex side under the vortex, very close to the wall (figure 19*e*). It sits in a region of high shear connected to the wall-normal gradient of the streamwise velocity and is not consistent with the known low-frequency 'z' mode in the steady-vortex case.

The higher-frequency regions found in the experiments of Lerche and Bippes (see figure 1) seem to reflect both 'z' and 'y' modes, although it is difficult to discern different modes. Note that the contribution of higher frequency ('y'-)modes is enhanced in this representation because the second time derivative has been employed. (Thereby, the amplitude of a single-frequency mode scales quadratically with its frequency.) Apart from that, the occurrence of a secondary-instability mode depends also on its intial amplitude, i.e. its content in the background disturbances. In this respect, the 'y' mode may be favoured by the turbulence level in the free stream, when compared to the 'z' mode that is situated closer to the wall. The DLR wind tunnel has indeed a larger turbulence level than the ASU tunnel, and in the latter a dominating 'z' mode has been found in the steady scenario as in our DNS with background disturbances excited at the wall.

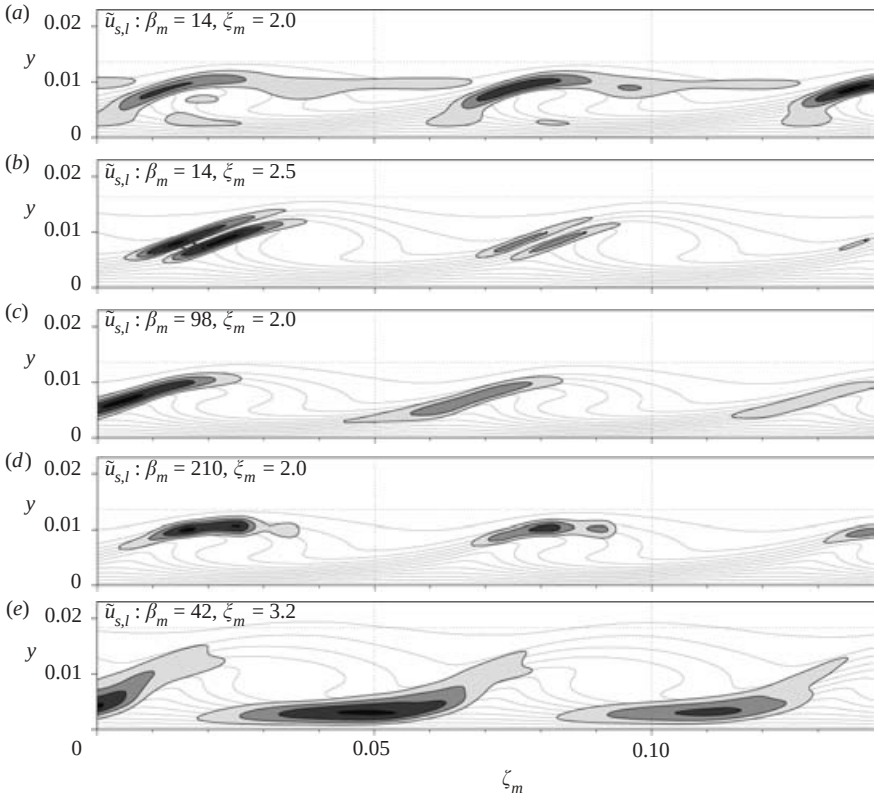

FIGURE 19. Isocontours of normalized $\tilde{u}_{s,l}$-amplitude for case WAVE + B in a crosscut in the moving system. Isolines from 0.35 to 0.95 with a 0.2 spacing are shown. The thin lines indicate the deformed mean flow, and the dotted lines the laminar boundary-layer edge. To scale.

The downstream amplification and spreading of the background wave packet in physical space is visualized by means of 'λ_2' isosurfaces in figure 20. (These isosurfaces identify vortical structures by locating a pressure minimum in a plane, see Jeong & Hussain 1995). The background disturbance input is at $\xi \approx 1.6$, upstream of the domain shown. At $t/T = 0.75$, the pulse disturbance is visible at $\xi \approx 2.55$, in between the skew primary vortical structures. At $t/T = 0.00$ a cascade of three small finger-like vortices twining around the left, upward moving side of the travelling primary crossflow vortex at $\xi \approx 2.7$ can be seen, with their axes aligned at about 20° to it (note the compression of the ξ-axis). The secondary vortices are co-rotating, anticlockwise when looking downstream, but in the opposite direction with respect to the primary vortices. By travelling downstream, an increasing number of 'finger' vortices appear with ongoing erosion of the primary vortex ($t/T = 0.25, 0.50$). However, the disappearance of the primary vortices downstream of $\xi = 3.2$ is partially due to a saturation-amplitude lowering also present without the pulse disturbances, cf. figure 10. The simultaneous visibility of at least two virtually equal finger-vortex cascades along the streamwise direction is an expression of the amplitude plateau in figure 18. Compared to case VORTEX, the individual finger vortices of a cascade have a larger streamwise spacing because the dominating frequency $\beta_m = 98$ is about 1.6 lower than in case VORTEX. Because they slide downstream along the skew crosswise travelling primary vortices, their effective direction of movement is

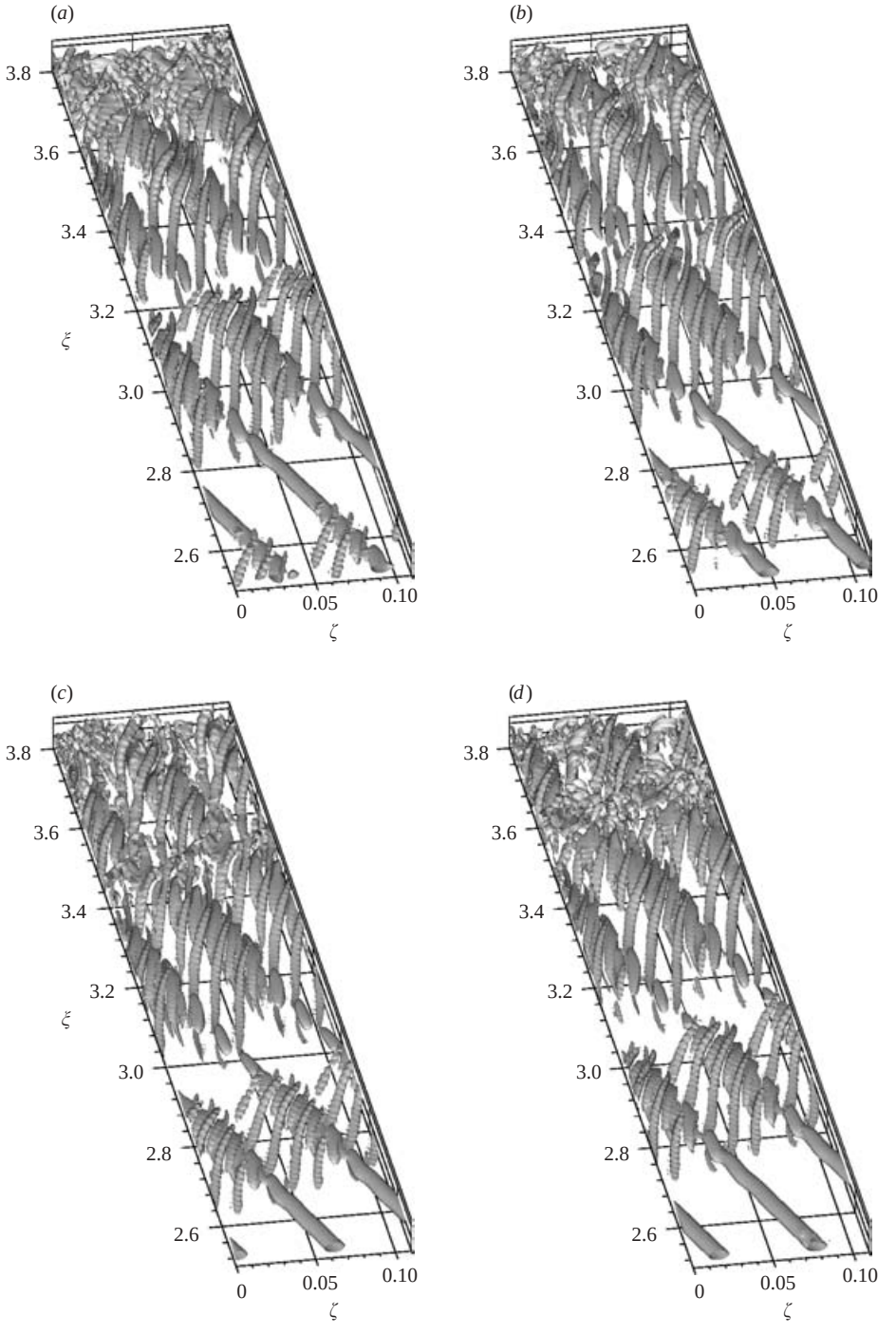

FIGURE 20. Visualization of vortical structures in the instantaneous flow fields for case WAVE + B, saturated crossflow wave plus periodic background pulses, by λ_2-isosurfaces, $\lambda_2 = -50$. (*a*) $t/T = 0.75$; (*b*) 0.00; (*c*) 0.25; (*d*) 0.50; T, period for $\beta = 14$. Approximately two spanwise wavelengths are shown; note the compression of the ξ-axis.

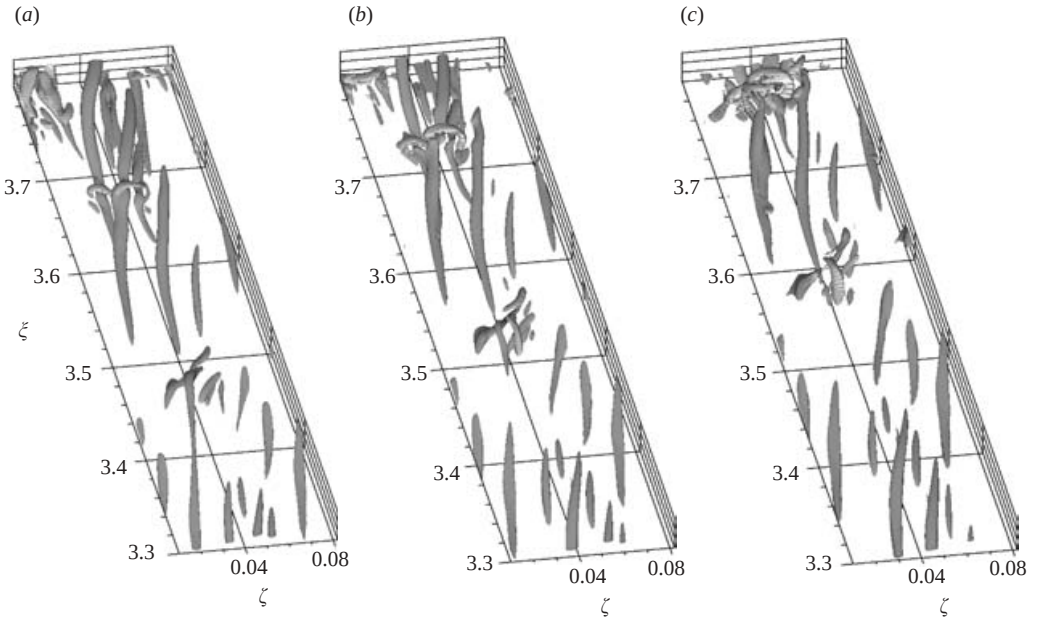

FIGURE 21. Visualization of vortical structures in the instantaneous flow fields for case WAVE + B, saturated crossflow wave plus periodic background pulses, by λ_2-isosurfaces, $\lambda_2 = -300$. T, period for $\beta = 14$; note the compression of the ξ-axis. (*a*) $t/T = 0.3$; (*b*) 0.4; (*c*) 0.5.

streamwise, similar to case VORTEX + B. Further downstream, the secondary finger vortices are stretched, and the downstream tips of an upstream cascade overlap the upstream ends of a preceding cascade.

Visualizing the vortical structures in a close-up of the relevant region with a higher λ_2-value for the isosurface (figure 21) reveals the mechanism responsible for the final breakdown. The secondary finger vortices strongly modulate the primary vortex during a saturated state, and finally the large primary structure breaks up into several smaller vortices still rotating clockwise. Those are somewhat under the finger vortices, but locally almost parallel to them. Thus, counter-rotating vortices of similar strength are present which form vortical bridges in between them ($\xi \approx 3.7$, $\zeta \approx 0.05$, at $t/T = 0.3$). Hairpin vortices evolve, a process known to cause the final randomization process. No clear vortical structure could be found connected to the mode with $\beta_m = 42$ close to the wall. It just seems to support the vortex split-up process. Contrarily, in case VORTEX + B the final breakdown is caused by tertiary vortices appearing within the closer-spaced finger vortices within a cascade. This process is obviously faster than the vortex split-up process observed in case WAVE + B. This explains the secondary-instability amplitude-saturation plateau prior to breakdown in the case of the travelling vortex.

6. Conclusions

Spatial direct numerical simulations have been used to investigate the nonlinear saturated state and the secondary instability mechanisms initiated by a single unsteady crossflow mode in a decreasingly accelerated three-dimensional flat-plate boundary layer. The most important results are:

(i) The forcing of a single unsteady crossflow mode with frequency β_1 and spanwise wavenumber γ_1 results in a periodic saturated state with crossflow vortices

travelling in the spanwise direction at constant speed β_1/γ_1. In the frequency-spanwise wavenumber spectrum this saturated state is given by the spectral modes $n(\beta_1, \gamma_1)$.

(ii) The travelling vortices possess a stronger streamwise vorticity component than their steady counterparts. They form strong shear layers inside the boundary layer, much closer at the wall, broader, and less tilted than steady vortices. These shear layers are dominated by the wall-normal gradient. Upon providing background disturbance pulses, a strong convective secondary instability mechanism is observed which globally is similar to the steady-vortex case.

(iii) To analyse the secondary instability mechanism unambiguously, an analysis method based on a Galilean-transformed coordinate system moving spanwise with the primary crossflow vortices is necessary.

(iv) For the secondary instability in the moving system, various modes can be identified, which are located at different positions inside the most pronounced shear layer. The amplification of the most unstable secondary mode, a kind of a so-called z-mode, is somewhat higher than known from steady-vortex induced regimes; its frequency is about 1.6 times lower, which is about seven times the primarily most unstable frequency.

(v) Each secondary mode in the moving coordinate system translates into a multi-frequency disturbance in physical space with a steady observer.

(vi) Unlike the steady-vortex scenario, a pronounced saturation appears for the secondary instabilities. Prior to final breakdown, a medium-frequency mode undergoes a second amplitude boost, ending the saturation stage.

(vii) Like the steady-vortex scenario, the natural disturbance selection leads to a packet of small finger vortices sliding downstream along the upper updraft side of the travelling priming vortex. Their streamwise spacing is larger than in the steady-vortex case. On travelling downstream, the secondary finger vortices persist for several primary streamwise wavelengths. They seem to modulate the priming vortex into an adapted group of smaller vortices, thus providing counter-rotating vortices to the finger vortices. Eventually the almost parallel counter-rotating vortices of similar strength locally connect, forming horseshoe type bridges, and turbulence is at hand.

(viii) The second medium-frequency amplitude rise occurs simultaneously with the 'modulation' process. This indicates an instability of the saturated secondary state originating from the lower downdraft side of the travelling primary vortex, supporting its break-up.

The financial support of this work by the Deutsche Forschungsgemeinschaft, DFG, under contract Kl 890/2 is gratefully acknowledged.

REFERENCES

Bippes, H. 1999 Basic experiments on transition in three-dimensional boundary layers dominated by crossflow instability. *Prog. Aerospace Sci.* **35**, 363–412.

Bonfigli, G. & Kloker, M. 1999 Spatial Navier–Stokes simulation of crossflow-induced transition in a 3-d boundary layer. In *New Results in Numerical and Experimental Fluid Dynamics II* (ed. W. G. Nitsche, H.-J. Heinemann & R. Hilbig), *Proc. 11. AG STAB/DGLR Symp. (1998)*, NNFM **72**, 61–68. Vieweg, Braunschweig.

Bonfigli, G. & Kloker, M. 2000 Three-dimensional boundary-layer transition phenomena investigated by spatial direct numerical simulations. In *Laminar-Turbulent Transition* (ed. H. Fasel & W. Saric), *Proc. IUTAM Symp. Sedona, AZ, USA (1999)*. Springer.

Deyhle, H. & Bippes, H. 1996 Disturbance growth in an unstable three-dimensional boundary layer and its dependence on environmental conditions. *J. Fluid Mech.* **316**, 73–113.

Haynes, T. S. & Reed, H. L. 1996 Computations in nonlinear saturation of stationary crossflow vortices in a swept-wing boundary layer. *AIAA Paper* 96-0182.

Haynes, T. S. & Reed, H. L. 2000 Simulation of swept-wing vortices using nonlinear parabolized stability equations. *J. Fluid Mech.* **405**, 325–349.

Högberg, M. & Henningson, D. 1998 Secondary instability of crossflow vortices in Falkner–Skan–Cooke boundary layers. *J. Fluid Mech.* **368**, 339–357.

Huai, X., Joslin, R. D. & Piomelli, U. 1999 Large-eddy simulation of boundary-layer transition on a swept wedge. *J. Fluid Mech.* **381**, 357–380.

Janke, E. & Balakumar, P. 2000 On the secondary instability of three-dimensional boundary layers. *Theoret. Comput. Fluid Dyn.* **14**, 167–194.

Jeong, J. & Hussain, F. 1995 On the identification of a vortex. *J. Fluid Mech.* **285**, 69–94.

Kawakami, M., Kohama, Y. & Okutsu, M. 1999 Stability characteristics of stationary crossflow vortices in three-dimensional boundary layer. *AIAA Paper* 99-0811.

Kloker, M. 1998 A robust high-resolution split-type compact FD scheme for spatial direct numerical simulation of boundary-layer transition. *Appl. Sci. Res.* **59**, 353–377.

Koch, W., Bertolotti, F. P., Stolte, A. & Hein, S. 2000 Nonlinear equilibrium solutions in a three-dimensional boundary layer and their secondary instability. *J. Fluid Mech.* **406**, 131–174.

Koch, W. 2002 On the spatio-temporal stability of primary and secondary crossflow vortices in a three-dimensional boundary layer. *J. Fluid Mech.* **456**, 85–111.

Kohama, Y., Kodashima, Y. & Watanabe, H. 1995 Randomization process in crossflow instability dominant three-dimensional boundary-layer transition. In *Laminar-Turbulent Transition* (ed. R. Kobayashi), *Proc. IUTAM Symp. Sendai, Japan (1994)*. Springer.

Lerche, T. 1996 Experimental investigations of nonlinear wave interactions and secondary instability in three-dimensional boundary-layer flow. In *Advances in Turbulence VI* (ed. S. Gavrilakis, L. Machiels & P. A. Monkewitz), *Proc. Sixth European Turbulence Conf., Lausanne, Switzerland (1996)*. Kluwer.

Lerche, T. 1997 Experimentelle Untersuchung nichtlinearer Strukturbildung im Transitionsprozess einer instabilen 3-d Grenzschicht. PhD thesis, published as Fortschrittbericht 310, Reihe 7 'Strömungstechnik', VDI Düsseldorf (1997), FRG.

Malik, M. R., Li, F. & Chang, C.-L. 1994 Crossflow disturbances in three-dimensional boundary layers: nonlinear development, wave interaction and secondary instability. *J. Fluid Mech.* **268**, 1–36.

Malik, M. R., Li, F. & Chang, C.-L. 1996 Nonlinear crossflow disturbances and secondary instabilities in three-dimensional boundary layers. In *Nonlinear Instability and Transition in Three-Dimensional Boundary Layers.* (ed. P. W. Duck & P. Hall), pp. 257–266. *Proc. IUTAM Symp. Manchester, UK (1995)*. Kluwer.

Malik, M. R., Li, F., Choudhari, M. M. & Chang, C.-L. 1999 Secondary instability of crossflow vortices and swept-wing boundary-layer transition. *J. Fluid Mech.* **399**, 85–115.

Reed, H. L., Haynes, T. S. & Saric, W. 1998 Computational fluid dynamics validation issues in transition modeling. *AIAA J.* **36**, 742–751.

Saric, W. S., Carrillo, Jr. & Reibert, M. S. 1998 Nonlinear stability and transition in 3-D boundary layers. *Meccanica* **33**, 471–489.

Saric, W. S., Reed, H. L. & White, E. B. 2003 Stability and transition of three-dimensional boundary layers. *Annu. Rev. Fluid Mech.* **35**, 413–440.

Spalart, P. R., Crouch, J. D. & Ng, L. L. 1994 Numerical study of realistic perturbations in 3-d boundary layers. In *Proc. AGARD Conf.: Application of Direct and Large Eddy Simulation to Transition and Turbulence*, AGARD-CP-551, 30.1–30.10, Chania, Crete, Greece.

Wassermann, P. & Kloker, M. 2002 Mechanisms and passive control of crossflow-vortex induced transition in a three-dimensional boundary layer. *J. Fluid Mech.* **456**, 49–84.

White, E. B. & Saric, W. S. 2003 Secondary instability of crossflow vortices. *J. Fluid Mech.* (submitted).

Wintergerste, T. & Kleiser, L. 1996 Direct numerical simulation of transition in a three-dimensional boundary layer. In *Transitional Boundary Layers in Aeronautics* (ed. R. A. W. M. Henkes & J. L. van Ingen), Proc. Colloquium of the Royal Netherlands Academy of Arts and Sciences, Amsterdam, NL (1995). North-Holland.

Wintergerste, T. & Kleiser, L. 1997 Breakdown of a crossflow vortex in a three-dimensional boundary layer. In *Direct and Large-Eddy Simulation II* (ed. J.-P. Chollet), pp. 179–190. Kluwer.